Image measurements of short-period gravity waves at equatorial latitudes

M. J. Taylor, W. R. Pendleton Jr., and S. Clark
Space Dynamics Laboratory and Physics Department, Utah State University, Logan

H. Takahashi and D. Gobbi
Instituto Nacional de Pesquisas Espaciais (INPE), São Jose dos Campos, São Paulo, Brazil

R. A. Goldberg
Laboratory for Extraterrestrial Physics, NASA Goddard Space Flight Center, Maryland

Abstract. A high-performance, all-sky imaging system has been used to obtain novel data on the morphology and dynamics of short-period (<1 hour) gravity waves at equatorial latitudes. Gravity waves imaged in the upper mesosphere and lower thermosphere were recorded in three nightglow emissions, the near-infrared OH emission, and the visible wavelength OI (557.7 nm) and Na (589.2 nm) emissions spanning the altitude range ~80–100 km. The measurements were made from Alcantara, Brazil (2.3°S, 44.5°W), during the period August–October 1994 as part of the NASA/Instituto Nacional de Pesquisas Espaciais "Guara campaign". Over 50 wave events were imaged from which a statistical study of the characteristics of equatorial gravity waves has been performed. The data were found to divide naturally into two groups. The first group corresponded to extensive, freely propagating (or ducted) gravity waves with observed periods ranging from 3.7 to 36.6 min, while the second group consisted of waves of a much smaller scale and transient nature. The later group exhibited a bimodal distribution for the observed periods at 5.18 ± 0.26 min and 4.32 ± 0.15 min, close to the local Brunt-Vaisala period and the acoustic cutoff period, respectively. In comparison, the larger-scale waves exhibited a clear tendency for their horizontal wavelengths to increase almost linearly with observed period. This trend was particularly well defined around the equinox and can be represented by a power-law relationship of the form $\lambda_h = (3.1 \pm 0.5)\tau_{ob}^{1.06\pm0.10}$, where λ_h is measured in kilometers and τ_{ob} in minutes. This result is in very good agreement with previous radar and passive optical measurements but differs significantly from the relationship $\lambda_h \propto \tau_{ob}^{1.5}$ inferred from recent lidar studies. The larger-scale waves were also found to exhibit strong anisotropy in their propagation headings with the dominant direction of motion toward the ~NE-ENE suggesting a preponderance for wave generation over the South American continent.

1. Introduction

Observations of gravity waves at equatorial latitudes are extremely rare. Gravity waves, particularly small-scale, short-period (<1 hour) waves, are known to be important drivers of the mean winds and thermal structure of the mesosphere and lower thermosphere via wave energy and momentum transport [e.g., *Fritts and Vincent*, 1987]. Variations in the seasonal flux of these waves are therefore expected to have marked effects on the dynamics of the upper middle atmosphere at equatorial, middle, and high latitudes. The statistical properties of small-scale gravity waves (at any latitude and season) are still uncertain, and measurements of their occurrence frequency, horizontal wavelengths, horizontal phase velocities (and hence their observed periods and dominant directions of motion) are of considerable importance for assessing their impact on the local atmospheric dynamics. In this paper we present image

measurements of an ensemble of 56 short-period wave events recorded in the visible and near-infrared (NIR) nightglow emissions. The measurements were made from Alcantara, Brazil (located on the magnetic equator at 2.3°S), as part of the NASA/Instituto Nacional de Pesquisas Espaciais (INPE) Guara campaign, and provide a rare opportunity to investigate the occurrence and dominant characteristics of short-period gravity waves in close proximity to the geographic equator.

To date, most nightglow imaging studies have utilized the bright NIR hydroxyl (OH) emission which originates from a well-defined layer (~8 km half width) centered at a mean altitude of ~87 km [*Baker and Stair*, 1988]. These observations have mainly been made from midlatitude mountain sites and have revealed a variety of wave motions. Classification of the waves into different groups has been attempted by several researchers [e.g., *Clairemidi et al.*, 1985; *Armstrong*, 1986; *Taylor*, 1986]. In most cases this classification has been based on a somewhat arbitrary division of the observed range of horizontal wavelengths (λ_h) which vary from typically $5 < \lambda_h < 100$ km. As a result of these studies, distinct spatial and temporal properties have emerged which suggest the existence of two

Table 1. Filter Details and Exposure Times for the Guara Campaign

Filter/Emission, nm	Bandwidth, nm	Transmission, %	Exposure Time, s	Altitude, km
OI (557.7)	2.67	81	90	96
Na (589.2)	2.37	81	120	90
OH* (715–930)	215	87	15	87
Bg (572.5)	2.65	83	90	⋯
OI (630.0)	2.33	83	180	280

*With a 20 nm notch at 865 nm to suppress the $O_2(0, 1)$ emission.

types (or groups) of short-period waves. The most prominent group, termed "bands," usually appears as an extensive series of quasi-monochromatic waves that exhibit horizontal wavelengths of a few to several tens of kilometers and phase speeds up to ~100 ms^{-1}. Band displays are quite persistent, lasting for typically a few hours, but it is not uncommon for them to endure for over 8 hours [e.g., *Taylor and Hill*, 1991]. Occasional studies have shown that this type of wave pattern is associated with the passage of freely propagating (or ducted) gravity waves most probably of tropospheric origin [e.g., *Taylor and Hapgood*, 1988; *Taylor et al.*, 1995a]. Recent measurements indicate that gravity waves associated with band patterns are as prevalent over oceans as they are over continental mountainous regions, suggesting weather disturbances rather than orographic forcing as their most likely source [*Taylor and Hill*, 1991; *Swenson et al.*, 1995; *Taylor et al.*, 1995a]. The second type of wave motion, termed "ripples," is distinct from bands in that ripples extend over much smaller geographic areas (typically <5 × 10^3 km^2) and usually exhibit considerably shorter lifetimes (<45 min) [*Peterson*, 1979]. Because of their transient nature, observations of ripples are comparatively few and have until now been restricted to measurements of their horizontal wavelengths which range from ~6 to 16 km [*Peterson and Adams*, 1983]. To our knowledge, only three ripple velocity measurements have been reported, suggesting relatively high horizontal phase speeds of 71 and 91 ms^{-1} [*Peterson*, 1979] and 46 ms^{-1} [*Taylor and Hill*, 1991].

The apparent similarity in morphology and dynamics of ripple events to the "billow" waves seen in noctilucent clouds (NLC) [e.g., *World Meteorological Organization (WMO)*, 1970], suggests similar-type source mechanisms [*Taylor*, 1986; *Clairemidi et al.*, 1985]. A likely source for ripples and billows is thought to result from the chance combination of wind and wave motions (of tidal or other origin) creating localized regions of strong wind shear which in turn generate small-scale waves in situ through the Kelvin-Helmholtz instability [e.g., *Haurwitz and Fogle*, 1969; *Taylor and Hapgood*, 1990]. This is a dynamic-type instability and in the absence of strong winds, or if the winds are aligned parallel to the perturbing wave, then the ripple structures should appear "spanwise" (i.e., oriented approximately parallel to the perturbing wave front). However, *Fritts et al.* [1993] have recently suggested an alternative three-dimensional, convective-type instability as a potential source for the generation of some of the smaller-scale (~5 km), shorter-lived (<several minutes) wave events. In this case and under similar wind conditions the resultant ripple structures will be "streamwise" oriented and should appear approximately perpendicular to the primary wave front. In principle, measurements of small-scale waves in the presence (and/or absence) of

larger-scale motions can therefore be used to discriminate between these source mechanisms.

With the development of sensitive solid state (CCD) imaging systems, measurements of gravity waves in the faint visible wavelength OI(557.7 nm) nightglow emission (peak altitude ~96 km) and the Na (589.2 nm) emission (peak altitude ~90 km) are now practical even from low-altitude sites. As these emissions peak at heights above the OH layer (peak altitude ~87 km), they enhance significantly the potential of image measurements for investigating the occurrence and properties of gravity waves that exist throughout the upper mesosphere and lower thermosphere (altitude range ~80–100 km). For the Guara campaign a multiwavelength, all-sky imaging system was used to record gravity waves over a large geographic area (>0.6 × 10^6 km^2) using sequential measurements of the NIR OH and visible wavelength OI and Na nightglow structure. Observations were made during two periods (6 August to 10 September and 1–16 October 1994) in conjunction with radar, photometer, and in situ rocket soundings.

In this study we present the results of the image analysis classifying the data into two categories using the "band" and "ripple" criteria defined earlier to determine the average properties of the quasi-monochromatic wave motions present at equatorial latitudes. The results have then been compared with previous gravity wave measurements at middle and low latitudes obtained by radar and lidar techniques [e.g., *Meek et al.*, 1985; *Reid*, 1986; *Gardner and Voelz*, 1987; *Manson*, 1990; *Beatty et al.*, 1992]. A clear tendency for the observed period of the bands to increase systematically with horizontal wavelength was found during the campaign. This trend was particularly well defined for the wave motions imaged around the equinox. Associated with this significant trend, a marked anisotropy in the distribution of wave azimuths was observed. The dominant direction of motion of the bands was found to be toward the equator from the SW–WSW suggesting frequent, recurring wave generation over the South American continent. In comparison, the ripple data exhibited an unusual bimodal distribution of horizontal wavelength with observed period.

2. Gravity Wave Imager

The image measurements were made using a large area (6.45 cm^2) solid state charged coupled device (CCD), consisting of 1024 × 1024 pixels, thermoelectrically cooled to −40°C. The high quantum efficiency (~80% at visible and 50% at NIR wavelengths) and low-noise characteristics of this device (dark current <0.5 e-/pixel/s) provide an exceptional capability for quantitative measurements of faint, low contrast (>5%) gravity wave signatures in the nightglow emissions. The camera was fitted with a fast (f/4) telecentric lens system and a five-position, temperature stabilized, filter wheel providing all-sky (180°) coverage using narrowband interference filters. The format of the all-sky lens system was such that each pixel in the CCD array subtended an equal angle on the sky resulting in an almost linear relationship between zenith angle and distance as measured from the center of the image. Table 1 lists the characteristics of the filters used for these measurements. Exposure times ranged from 15 s for the bright OH emission to 90 s and 120 s, respectively, for the fainter OI(557.7 nm) and NaD lines. As part of the image sequence, two additional measurements were made, one at 572.5 nm to assess the background sky conditions and the other at 630 nm to investigate the high
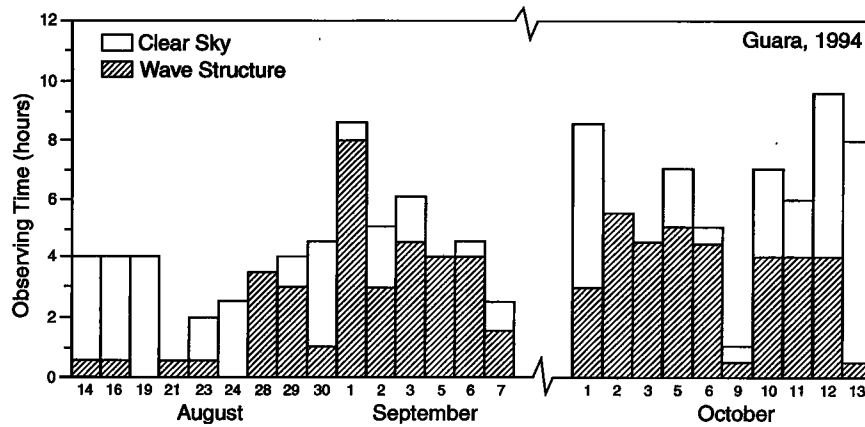
Figure 1. Frequency of occurrence of wave structure (bands and ripples) and "clear sky" observing hours for the Guara campaign. Approximately 120 hours of useable data were obtained during two periods: 6 August to 10 September and 1–16 October 1994.

altitude (~280 km) F-region OI(630.0 nm) emission (the results of which will be the subject of a separate report.

For this study the background images were used to help discriminate the presence of tropospheric cloud in the data. More detailed spectral analyses utilize the background images to subtract out the effects of scattered light (mainly from the city of Sao Luis ~40 km away) and airglow continuum emission from the data images prior to analysis. Observations of each nightglow emission were recorded once every ~9 min except for the OI(557.7 nm) emission which was sampled every 4–5 min. For a pure monochromatic wave motion this implies a limiting Nyquist period of 18 min for the OH and ~9–10 min for the OI(557.7 nm) emissions. However, spatial nonuniformities in the waveforms, such as "fronts" or "edges," often enable us to accurately track the motion of individual waveforms and hence to evaluate wave periods significantly less than the Nyquist limit.

3. Analysis and Results

3.1. Guara Image Measurements

The imaging system was located at the INPE Satellite Tracking Station, Centro de Lancamento de Alcantara, Brazil (2.3°S, 44.5°W). Measurements were made in conjunction with the NASA/INPE Guara campaign during two observing periods: 6 August to 10 September, as part of the "MALTED" program [*Goldberg et al.*, 1995], and 1–16 October, as part of the "SPREAD F" program. Although the measurements were made from approximately sea level, a wealth of high contrast, short-period wave structure was recorded during both observing periods. This result is depicted in Figure 1 which plots the frequency of occurrence of wave structure at any position within the "all-sky field," for the OI(557.7 nm) image data. In practice, the useful field of view was found to extend down to zenith angles of ~80° (limited primarily by local horizon and tropospheric scattering and extinction effects). This corresponds to an effective ground range of ~480 km for the OI emission assuming a mean altitude of 96 km. Depending on the orientation of the waveforms, the cutoff for identifying periodic structure at this limiting range is ~20 km. Despite the sometimes severe restrictions imposed by meteorological cloud, approximately 120 hours of useable data were recorded on 23 out of 25 nights, of which ~70 hours contained distinct wave struc-

ture indicating a relatively high frequency of occurrence (~60%).

Figure 2 shows four examples of the gravity waves imaged during this campaign. In Figure 2a a well-developed extensive OI(557.7 nm) band display is evident. This wave pattern exhibited a horizontal wavelength λ_h = 32.0 ± 0.9 km and a phase speed v_h = 67 ± 1 ms^{-1} indicating an observed period τ_{ob} = 8.0 ± 0.3 min. The waves were observed for more than 5 hours as they progressed toward the ~NE. Figure 2b illustrates a similar wave pattern recorded in the NIR OH emission approximately one month later. In this example over 11 near-linear wave crests of average λ_h = 18.2 ± 0.3 km were
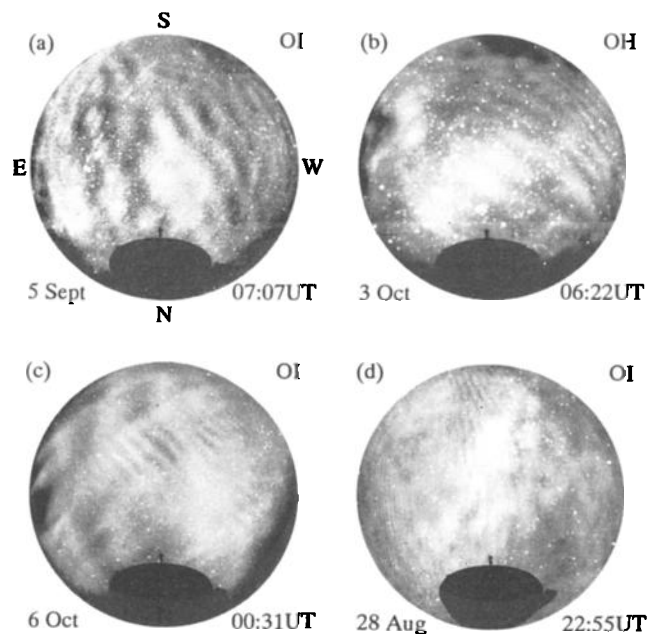

Figure 2. Four images showing examples of gravity wave structure recorded in the OI(557.7 nm) and near-infrared OH emissions during the campaign: (a, b) extensive bands; (c) example of transient ripples; (d) a complex mixture of band and ripple waves. Note that the oval silhouette at the bottom of each image is the Instituto Nacional de Pesquisas Espaciais satellite tracking antenna, while the dark patches at low elevations in Figures 2b and 2c are clouds.
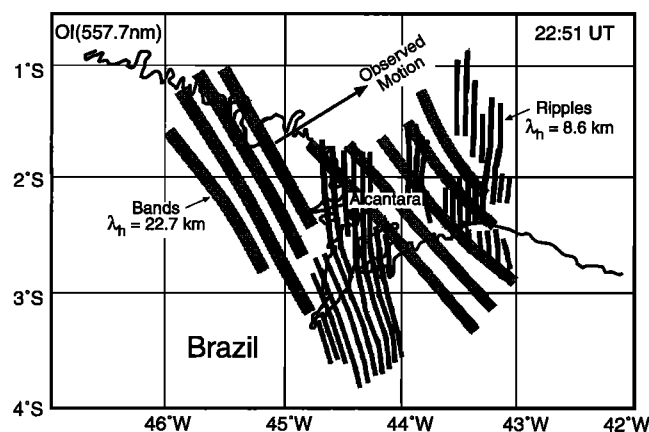
Figure 3. Map showing the geographic location and orientation of the complex OI(557.7 nm) band and ripple display shown in Figure 2d. The data are plotted for an assumed emission height of 96 km.

imaged as they progressed toward the ~NNE on a similar heading to the bands shown in Figure 2a.

Figure 2c shows an example of a ripple display. During the Guara campaign over 25 ripple events were recorded yielding

novel measurements of their velocities and observed periods. In this example the ripples were imaged in the OI(557.7 nm) emission and exhibited a mean $\lambda_h = 12.0 \pm 0.3$ km and an average $v_h = 35.4 \pm 1.4$ ms^{-1}, yielding a $\tau_{ob} = 5.6 \pm 0.3$ min. More complex wave patterns consisting of a mixture of two (or more) band patterns or band and ripple displays were observed on several occasions during this campaign. The OI (557.7 nm) image of Figure 2d shows an extensive set of N-S aligned ripples in the zenith and eastern sky ($\lambda_h = 8.6 \pm 0.1$ km) superposed on a faint band pattern ($\lambda_h = 22.7 \pm 0.6$ km) that was observed to progress from low elevations toward the equator, again on an ~ENE heading. The geographic location, orientation, and the relative scale sizes of these two wave displays are shown in the map of Figure 3 which also illustrates the observing geometry for these measurements.

3.2. Equatorial Wave Characteristics

Analysis of this data set has focused on identifying wave events, primarily in the OI(557.7 nm) emission (peak altitude ~96 km), with a subsequent investigation of the lower-altitude NaD (589.2 nm) and NIR OH emissions to determine additional events that were not evident in the OI data set. The images were calibrated first using the star background, and then prominent wave features were mapped onto the Earth's surface to form a series of maps (e.g., Figure 3), from which the

Table 2. Chronological List of Measured Wave Parameters (λ_h, v_h, τ_{ob}) for Band Events and Calculated Values for $(\tau_i)_m$ and $(\lambda_z)_m$ Using Model Winds

Band Event	Date	Layer	λ_h, km	v_h, ms^{-1}	τ_{ob}, min	Azimuth, °N	τ_b, min	$(\tau_i)_m$, min	$(\lambda_z)_m$, km
1	28 Aug.	OI	22.7	36	10.4	60	(5.10)	15	8.0
2	29 Aug.	OH	16.4	27	10.0	170	(5.10)	12	7.5
3	29 Aug.	OI	25.4	49	8.6	160	(5.10)	9.3	17
4	30 Aug.	OH	18.4	26	11.9	80	5.10	13	8.1
5	30 Aug.	OH	17.6	20	14.9	50	5.10	14	6.9
6	30 Aug.	OI	30.9	49	10.5	270	5.10	8.1	25
7	1 Sept.	OI	15.7	38	6.9	210	5.14	6.0	26
8	1 Sept.	OI	23.6	62	6.4	210	5.14	5.8	45
9	1 Sept.	OI	27.5	33	13.7	140	5.14	20	7.3
10	1 Sept.	OI	27.9	55	8.4	100	5.14	12	14
11	1 Sept.	OI	20.6	33	10.3	110	5.14	18	6.1
12	1 Sept.	Na	30.8	14	36.7	255	5.14	20	8.2
13	1 Sept.	OH	18.2	27	11.1	335	5.14	8.8	13
14	2 Sept.	OH	13.8	63	3.7	55	5.21	3.6	?
15	2 Sept.	OH	20.7	41	8.4	60	5.21	8.2	17
16	3 Sept.	OH	13.9	57	4.1	80	5.03	4.2	?
17	3 Sept.	OI	39.4	71	9.3	65	5.03	11	19
18	5 Sept.	OI	26.6	61	7.2	70	5.13	9.3	18
19	5 Sept.	OI	32.0	67	8.0	95	5.13	10	18
20	5 Sept.	OH	15.4	46	5.6	50	5.13	5.1	?
21	5 Sept.	OI	37.6	56	11.2	60	5.13	14	14
22	6 Sept.	OI	15.6	54	4.8	50	5.24	6.0	28
23	7 Sept.	OI	38.3	56	11.5	65	5.14	15	14
24	1 Oct.	OI	17.5	68	4.3	355	5.02	4.3	?
25	2 Oct.	OI	41.7	59	11.8	60	(5.02)	16	13
26	3 Oct.	OH	18.2	...	...	...	...	...	...
27	5 Oct.	OI	31.0	62	8.3	310	5.15	7.0	34
28	5 Oct.	OI	25.2	61	6.9	70	5.15	9.9	15
29	10 Oct.	OI	20.3	42	8.2	160	5.26	8.6	16
30	11 Oct.	OI	19.6	53	6.2	315	5.29	5.2	?
31	11 Oct.	OI	31.7	55	9.6	150	5.29	11	18

The date listed corresponds to the evening when the measurements were initiated. Values of τ_b were deduced from O$_2$ and OH temperature measurements using a tilting filter photometer; values in parentheses are estimated. The space between events 13 and 14 indicates the division into two sets corresponding to the onset of strong anisotropy in the wave headings (i.e., prior to and after 2 September). The question mark indicates situations where a value for $(\lambda_z)_m$ is indeterminate using equation (2) as the estimated intrinsic period was less than τ_b.

Table 3. Chronological List of Measured Wave Parameters $(\lambda_h, v_h, \tau_{ob})$ for Ripple Events

Ripple Event	Date	Layer	λ_h, km	v_h, ms^{-1}	τ_{ob}, min	Azimuth, °N	τ_b, min
1	17 Aug.	OI	16.1	41.5	6.5	130	...
2	17 Aug.	OH	16.0	51.4	5.2	135	...
3	17 Aug.	OH	9.8	...	...	...	...
4	17 Aug.	OH	10.5	...	...	...	...
5	17 Aug.	OH	9.5	...	...	...	...
6	22 Aug.	OI	14.9	43.8	5.7	110	...
7	28 Aug.	OI	8.6	...	...	...	...
8	1 Sept.	OI	10.3	62.0	2.8	210	5.14
9	1 Sept.	OI	10.2	29.9	5.7	110	5.14
10	1 Sept.	OI	12.8	38.9	5.5	75	5.14
11	1 Sept.	Na	11.3	27.3	6.9	200	5.14
12	1 Sept.	OH	7.5	29.7	4.2	180	5.14
13	1 Sept.	OH	6.0	23.3	4.3	175	5.14
14	2 Sept.	OH	8.2	24.9	5.5	80	5.21
15	5 Sept.	OH	10.2	40.7	4.2	130	5.13
16	3 Oct.	OI	11.4	25.4	7.5	20	...
17	3 Oct.	OI	17.8	69.6	4.3	40	...
18	5 Oct.	OI	14.1	85.9	2.7	180	5.15
19	6 Oct.	OI	12.0	35.4	5.6	40	5.20
20	6 Oct.	OI	12.3	48.6	4.2	30	5.20
21	10 Oct.	OI	17.7	53.9	5.5	0	5.26
22	11 Oct.	OI	12.8	47.7	4.5	170	5.29
23	11 Oct.	OI	7.0	...	...	...	5.29
24	12 Oct.	OI	15.3	47.5	5.4	340	5.30
25	12 Oct.	OI	10.0	...	...	...	...

Note that on six occasions it was not possible to determine the wave phase speed accurately. Values of τ_b are listed (where available) for comparison with the deduced τ_{ob} for the 19 events. As in Table 2, the space indicates the division into two groups.

horizontal parameters $(\lambda_h, v_h, \tau_{ob})$ and the wave propagation heading were determined for each identifiable event. (Note that very low contrast features that were not easily identifiable in the data have not been included in this analysis.) A full description of this spatial analysis procedure (as applied to narrow angle image data) has been given by *Hapgood and Taylor* [1982]. This method of analysis was determined to be the most practical, in this case, as attempts to perform two-dimensional spectral analysis of the wave motions (as described by *Taylor and Garcia* [1995] were often impeded by transient clouds. The results of the spatial analysis were then separated into two groups corresponding to bands and ripples using the differences in the geographical extent and the duration of each wave pattern as the primary dividing criteria. A total of 37 OI(557.7 nm) displays were analyzed in this manner, 21 of which consisted of extensive band motions (often, but not always, occupying the entire field of view), with 16 small-scale, short-duration ripple events. In addition, 17 OH displays (9 bands and 8 ripples) and 2 Na(589.2 nm) displays (1 band, 1 ripple) were observed totaling 56 wave events. Because of clouds the number of displays yielding accurate measurements of wave velocity was reduced to 49 events. For comparison, a summary of the measured band and ripple parameters is given in Tables 2 and 3, respectively. On some occasions the wave activity was very high, and several band and/or ripple events were imaged during a single night (e.g., September 1). However, bands and ripples were not always present on the same nights.

Figure 4 plots the distribution of horizontal wavelengths for the bands and ripples as a function of their occurrence frequency. The data have been binned into histograms of 5 km width (which is well within the typical measurement accuracy of ±3% corresponding to <±1 km) to determine the most frequently observed horizontal scale sizes. The strong tendency

for ripples (Figure 4b) to occur over a very narrow wavelength range is immediately apparent with ~83% of all events having wavelengths in the 5–15 km range. In contrast, the band displays exhibited a significantly broader range of horizontal wavelengths extending from ~10–45 km (Figure 4a) and ~94% of all bands had wavelengths >15 km. The average band wavelength was 24.3 km, approximately twice that of the ripples at 11.7 km.

Figure 5 shows the corresponding distribution of wave speeds (for 49 events) plotted at 10 ms^{-1} intervals (typical individual measurement error ±5% or <±3 ms^{-1}). The band measurements (Figure 5a) range from 14 to 71 ms^{-1} and exhibit an average value of 48 ms^{-1}. However, there is a clear tendency for many of the waves in this data set to exhibit relatively high phase speeds, with the highest frequency of occurrence in the 50–60 ms^{-1} range. Surprisingly, the ripples (Figure 5b) exhibited a similar distribution range to the bands (23–86 ms^{-1}) and an almost identical average speed of 44 ms^{-1}. No obvious tendency toward high phase speeds was found. The resulting distribution of observed wave periods (binned at 2 min intervals) is given in Figure 6. The ripples exhibit a remarkably sharp distribution centered on the 4–6 min bin (with ~74% of events occurring within this range) and an average wave period 5.1 min. In comparison, the distribution of band periodicities is considerably broader than for the ripples and shows a clear tendency toward longer wave periods (with 83% of bands exhibiting periods >6 min) and a significantly higher average value of 9.6 min (approximately twice that of the ripples).

3.3. Distribution of Wave Headings

The propagation headings for both wave groups, summed over 15° intervals, are plotted in Figure 7. The distribution of
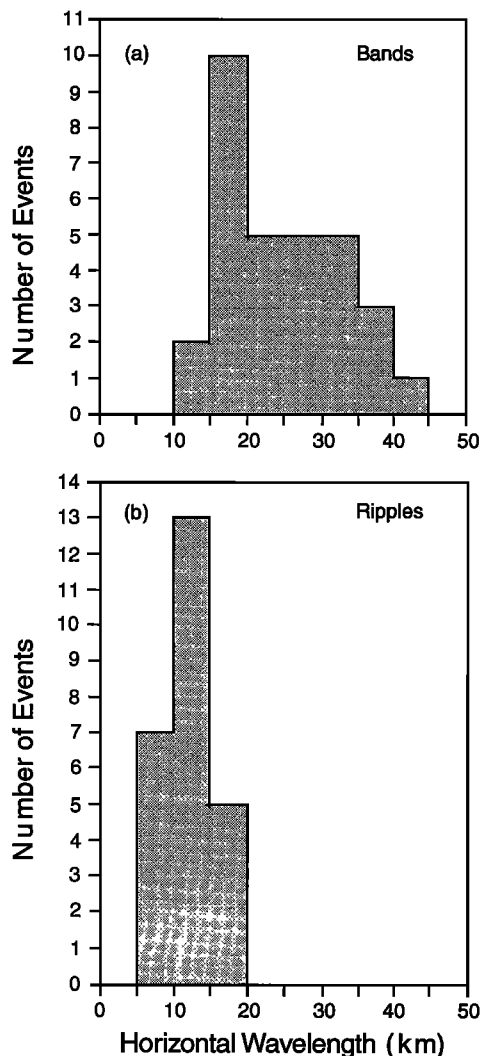
Figure 4. Histogram plots showing the distribution of horizontal wavelengths for (a) bands and (b) ripples as a function of number of wave events. Note the strong tendency for short horizontal wavelengths for the ripples.

fore occurred on and after 2 September. The ripple data (Figure 8b) also indicate a distinct change in their meridional (but not zonal) components of motion prior to and after this date, with a clear preference for southward wave progression during the first interval followed by a reversal to northward progression (in all but two cases) during the second interval.

3.4. Wavelength-Period Trends

Prior to considering possible trends involving spatial scales and observed periods, it is important to distinguish between the measured and the derived quantities and to mention analysis procedures. For nightglow imaging studies, the measurements yield directly (λ_h, v_h) pairs. The measured λ_h (typical measurement uncertainty of $\pm3\%$) is an intrinsic wave parameter, whereas v_h (typical error bars of $\pm5\%$) is an observed phase velocity, which usually differs from its intrinsic counterpart because of background winds. These parameters are used to derive τ_{ob} (typical error bars of $\pm6\%$) from the ratio (λ_h/v_h). Since values of τ_{ob} are derived from this ratio, it is important to examine first the distribution of (λ_h, v_h) pairs for the band and ripple events before considering possible trends in their horizontal and vertical scales with observed period. Figure 9 shows a (λ_h, v_h) scatter diagram for all of the wave events listed in Tables 2 and 3. Each point is associated with a τ_{ob} which is the same as the intrinsic period when Doppler-shifting effects are negligible. The ripple events (crosses) exhibit a visually significant positive trend which is expected, based on the sharply peaked distribution of observed periods in the histogram of Figure 6b. However, an interesting feature, not apparent in the histogram plot, is a strong tendency toward a bimodal trend for the ripples, suggesting two preferred peri-
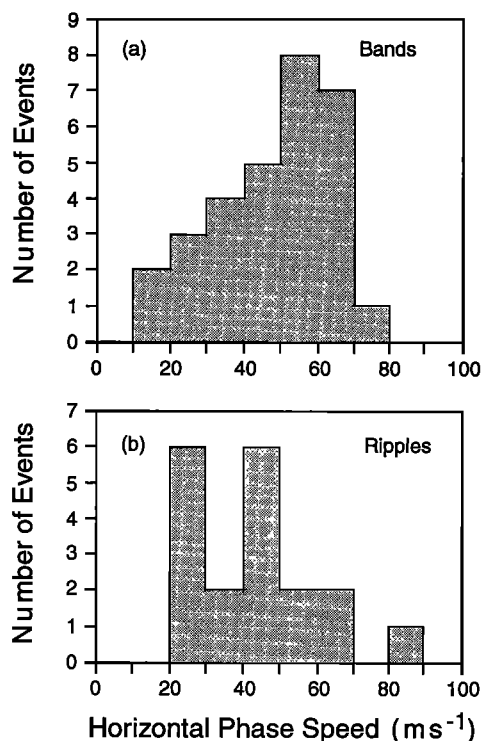
bands (Figure 7a) is highly anisotropic, exhibiting a strong preference (12 events) for wave progression toward the ~NE-ENE (azimuth range ~45°–75°). In contrast, the ripples (Figure 7b) indicate a much broader range of propagation azimuths with an underlying tendency for eastward phase progression (with 13 out of 19 events exhibiting an eastward component of motion). Figure 8 depicts the velocity distribution of the two wave groups. Although the phase speeds of the bands and ripples varied considerably (from ~10 to ~90 ms^{-1}), there is no obvious evidence of an azimuthal bias for faster or slower wave motions. For reasons that are discussed later (section 4), each plot has been divided into two parts: the dashed arrows indicate the velocity vectors for all wave events observed prior to 2 September, while the solid arrows represent wave vectors recorded on and after this night. The band azimuths (Figure 8a) appear to be randomly distributed prior to 2 September. However, measurements on subsequent nights indicate a major change in their azimuthal distribution with a large number of displays (>65%) exhibiting motion toward the ~NE-ENE. The majority of the wave events responsible for the strong anisotropy in the band headings (Figure 7a) there-

Figure 5. Histogram plots showing the distribution of observed horizontal phase speeds for (a) bands and (b) ripples as a function of number of wave events. Note the similar range of phase speeds in each case.

odicities. This feature is also apparent in Figures 10 and 12 (which present λ_h and v_h as a function of τ_{ob}) and is discussed in more detail in section 4.4.

Initial inspection of the band events of Figure 9 indicate that they are almost randomly distributed. However, when coded to conform to the division indicated in the velocity distribution data (Figure 8), it is clear that the distribution of (λ_h, v_h) pairs observed prior to 2 September (open circles) is significantly different from that observed after this date (solid circles). The mean λ_h values for the two distributions are comparable, at 23 and 26 km, respectively. However, the mean horizontal phase speed of the waves observed ≥ 2 September is significantly higher (~ 57 ms^{-1}) than that observed earlier in the campaign (~ 36 ms^{-1}). Furthermore, the spread in the values about each mean is much larger for the waves observed prior to 2 September than after this date (fractional standard deviations of 0.39 and 0.15, respectively). Together, these observations suggest markedly different source and/or propagation conditions during these two observing intervals.

Figure 10 summarizes the Guara image results in a plot of the intrinsic λ_h as a function of τ_{ob}. As in the previous figure, the bands are marked by the open and solid circles and the
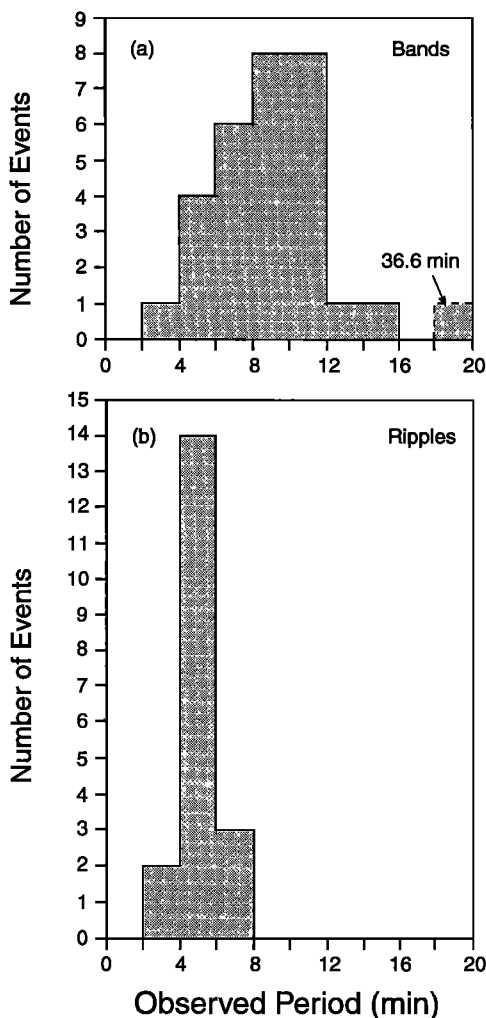

Figure 6. Histogram plots showing the distribution of observed wave period for (a) bands and (b) ripples as a function of number of wave events. Note the prominent peak in the ripple data at ~ 5 min.
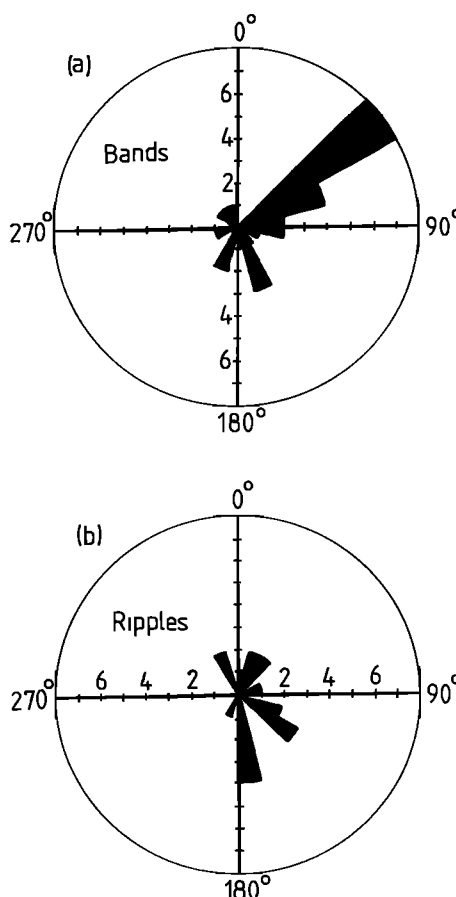

Figure 7. Plot showing the distribution of wave headings (summed over 15° intervals) for (a) bands and (b) ripples. Note the strong preference for bands to progress toward the $\sim$NE-ENE.

ripples by the crosses. In this format all of the ripple events are seen to reside in a small cluster bounded by wavelength limits of 5–20 km and periods between 2 and 8 min. In comparison the bands exhibit a clear tendency for larger values of λ_h with increasing τ_{ob}. The range of horizontal wavelengths for a given τ_{ob} also increases significantly as τ_{ob} increases. To investigate trends in the data, the three wave components identified in Figure 10 (i.e., ripples, bands ≤ 1 September and bands ≥ 2 September) are presented in individual scatter diagrams (in log-log format) in Figure 11. Regression analyses were carried out following procedures similar to those described by *Wonnacott and Wonnacott* [1981]. An examination of the deviations associated with λ_h and τ_{ob} revealed similar fractional values which greatly exceed the experimental uncertainties. Hence, for this study, an estimation technique was adopted which accounted for significant stochastic variability in both λ_h and τ_{ob}. In Figure 11c the dashed line through the distribution reflects the weighted two-way regression corresponding to a power-law model of the form $\lambda_h = A \tau_{ob}^B$. The power-law model was selected to facilitate comparison with results from other similar-type investigations using radar and lidar data where this model has been widely used [e.g., *Reid*, 1986; *Reid and Vincent*, 1987; *Gardner and Voelz*, 1987]. However, in the present study, the modest ranges in the pertinent variables contributed to very similar confidence levels for both linear and power-law regression analyses.
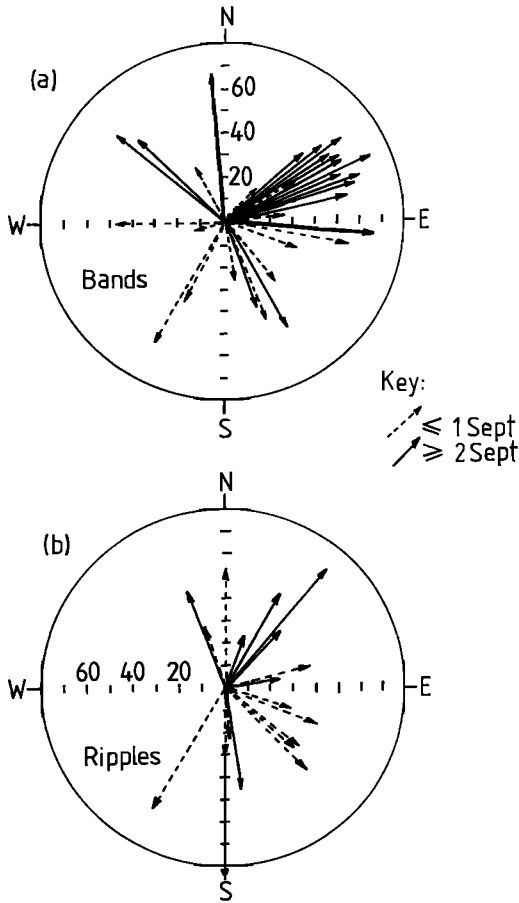
Figure 8. Two plots showing the velocity distribution of the waves for (a) bands and (b) ripples. The dashed vectors denote waves recorded prior to 2 September, while the solid arrows show the waves imaged on and after this date. The direction of motion of the waves was usually determined to within an accuracy of typically ±5°. Note the strong preference for band motion toward the ~NE-ENE after 2 September.
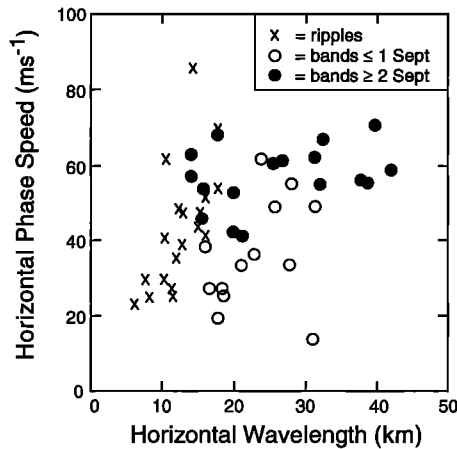

Figure 10. Plot of horizontal wavelength as a function of observed wave period for the band (and ripple data). Note the clear tendency for the bands to increase in wavelength with larger observed period and the bimodal clustering of the ripples around ~5 min period.

The ripple data in Figure 11a exhibit a very weak positive trend with a squared correlation coefficient (r^2) of $\sim 10^{-2}$. In this case, the trend is insignificant since the probability of obtaining this value of r^2 by chance, with $N = 19$ pairs of

Figure 9. Scatter diagram showing the distribution of $(\lambda_h - v_h)$ pairs for the band and ripple data. The bands have been divided into two groups (before and after 2 September) according to the onset of strong directionality in the wave headings.
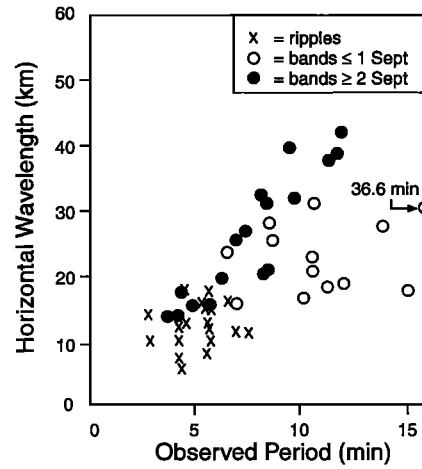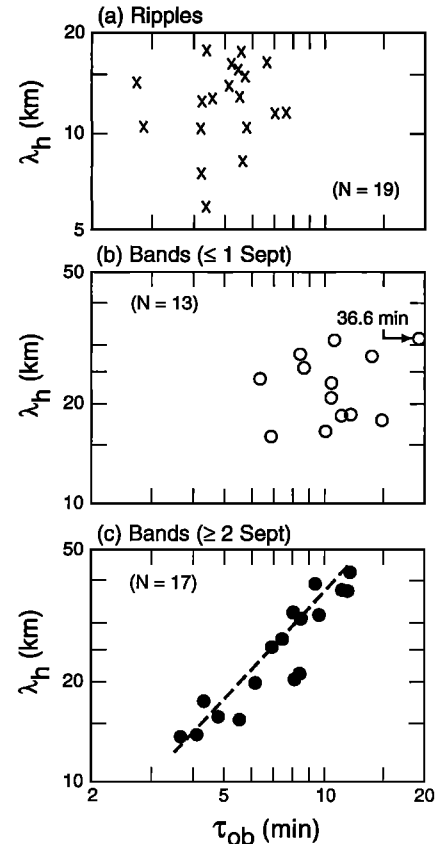

Figure 11. Log-log plots showing the data of Figure 10 divided into three groups: (a) ripples, (b) bands ≤1 September, and (c) bands ≥2 September. The dashed line in Figure 11c indicates the best fit power law model $\lambda_h = (3.1 \pm 0.5)\tau_{ob}^{1.06 \pm 0.10}$.

Table 4. Results of Correlation Analysis of Figure 11 for Band and Ripple Events

Type of Wave Motion	Power Law Coefficient, A	Power Law Exponent, B	Square of Correlation Coefficient, r^2	Total Data Pairs, N	Measurement Probability, P^*	Standard Deviation	
						σ_A	σ_B
All bands	3.9	0.86	0.29	29	$<3 \times 10^{-3}$	1.0	0.40
Bands $\geq$ 2 Sept.	3.1	1.06	0.85	17	$<10^{-4}$	0.5	0.10
Bands $\leq$1 Sept.	$\cdots$	$\cdots$	$\sim 10^{-3}$	12	~ 1	$\cdots$	$\cdots$
Ripples	$\cdots$	$\cdots$	$\sim 10^{-2}$	19	~ 0.5	$\cdots$	$\cdots$

Parameters A and B were calculated using a weighted two-way regression analysis of the form $\lambda_h = A\tau_{ob}^B$. Note that the data point at (36.6 min, 30.8 km) was not used in the analysis since its parameters did not satisfy Chauvent's criterion.

*Indicates the probability of obtaining the given values of r^2 by chance.

observations, is $\sim$0.5. Similarly, the data points in Figure 11b, which represent the band data for the period $\leq$ 1 September, exhibit no significant trend. In sharp contrast, the data in "Figure 11c" (bands $\geq$2 September) are characterized by a highly significant ($r^2 = 0.85$ with $N = 17$) positive trend ($B = 1.06 \pm 0.10$). The Student's t-test for this case is consistent with a very small probability ($<10^{-4}$) that this level of correlation resulted purely by chance. We have also performed a correlation analysis for the full set of band data which, as expected, is also highly significant (measurement probability of $<3 \times 10^{-3}$). The resultant power-law coefficient in this case ($B = 0.86 \pm 0.4$) was found to be the same as that determined from the band data of Figure 11c given the analysis uncertainties. This trend in the band data is essentially linear for the short-period gravity waves under consideration here. The scaling factor (coefficient A) relating λ_h to τ_{ob} was found to lie in the range $\sim$3–4. Thus a wave with a τ_{ob} close to the local Brunt-Vaisala period of $\sim$5 min would be expected to exhibit a horizontal wavelength of $\sim$15–20 km, whereas a $\sim$20-min period band pattern will have a λ_h of typically $\sim$50–70 km. For, convenience, the results of the correlation analyses (A, B, r^2) are summarized in Table 4, where the standard deviations for the parameters A and B are given only for the highly significant correlations.

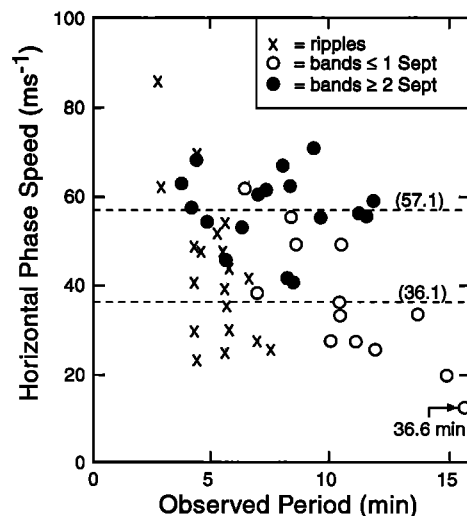Figure 12 plots the observed horizontal phase speeds v_h as a

Figure 12. Plot showing the distribution of horizontal phase speed as a function of observed period. The two dashed lines indicate the mean phase speeds for the bands imaged prior to 2 September (36.1 ms^{-1}) and after this date (57.1 ms^{-1}).

function of τ_{ob}. The previously noted tendency (Figure 9) for the ripple events to be associated with two distinct observed periods, one slightly above and the other just below the mean value of $\sim$5 min, is most apparent (with 14 of the 19 events forming two vertical columns). The difference in the average speed of the bands observed prior to and after 2 September (indicated by the dashed lines) is a key feature of Figure 12. All of the events recorded $\geq$2 September are characterized by relatively high and similar values of v_h (range 41.0–70.6 ms^{-1}), whereas those events observed prior to this date are characterized by significantly lower values of v_h and a somewhat larger spread (range 14.0–61.7 ms^{-1}). The implications of this difference are considered in more detail (section 4.2) when the results for the inferred vertical wavelengths are discussed.

4. Discussion

Bands were the most prevalent type of wave structure imaged in each of the three nightglow emissions (OI, OH, and Na) investigated. Many of these wave displays were extensive and are considered to be the signature of freely propagating, short-period gravity waves [e.g., Taylor et al., 1987]. However, recent joint radar and imaging studies performed at low latitudes ($\sim$20°N) have revealed a tendency for this type of wave motion to be Doppler ducted by the background winds at mesospheric heights (J. R. Isler, private communication, 1996). Depending upon the prevailing wind conditions during the Guara campaign, a significant percentage of the short-period wave events imaged may also have encountered mesospheric ducting thereby increasing their horizontal range of propagation from the source. In general, the range of values (λ_h, v_h, τ_{ob}) present in the Guara equatorial data (bands and ripples) compare favorably with the ensemble of observations recorded at higher latitudes using similar-type instrumentation. However, a tendency toward larger mean values for the horizontal wavelength ($\approx$40 km) and longer observed periods is apparent in some midlatitude band-type data [e.g., Armstrong, 1982; Moreels and Herse, 1977; Herse et al., 1989; Swenson and Mende, 1994; Fagundes et al., 1995; Taylor et al., 1995b]. Significantly, the mean band wavelength during the Guara campaign was 24.3 km and only one event exhibited a $\lambda_h > 40$ km. Furthermore, all but one of the Guara displays manifested observed periods $<$16 min which are substantially lower than many previous reports from midlatitudes. These results may herald some potentially significant differences in the dominant characteristics of short-period equatorial gravity waves compared with those regularly seen at higher latitudes, possibly associated with variations in their most copious sources.
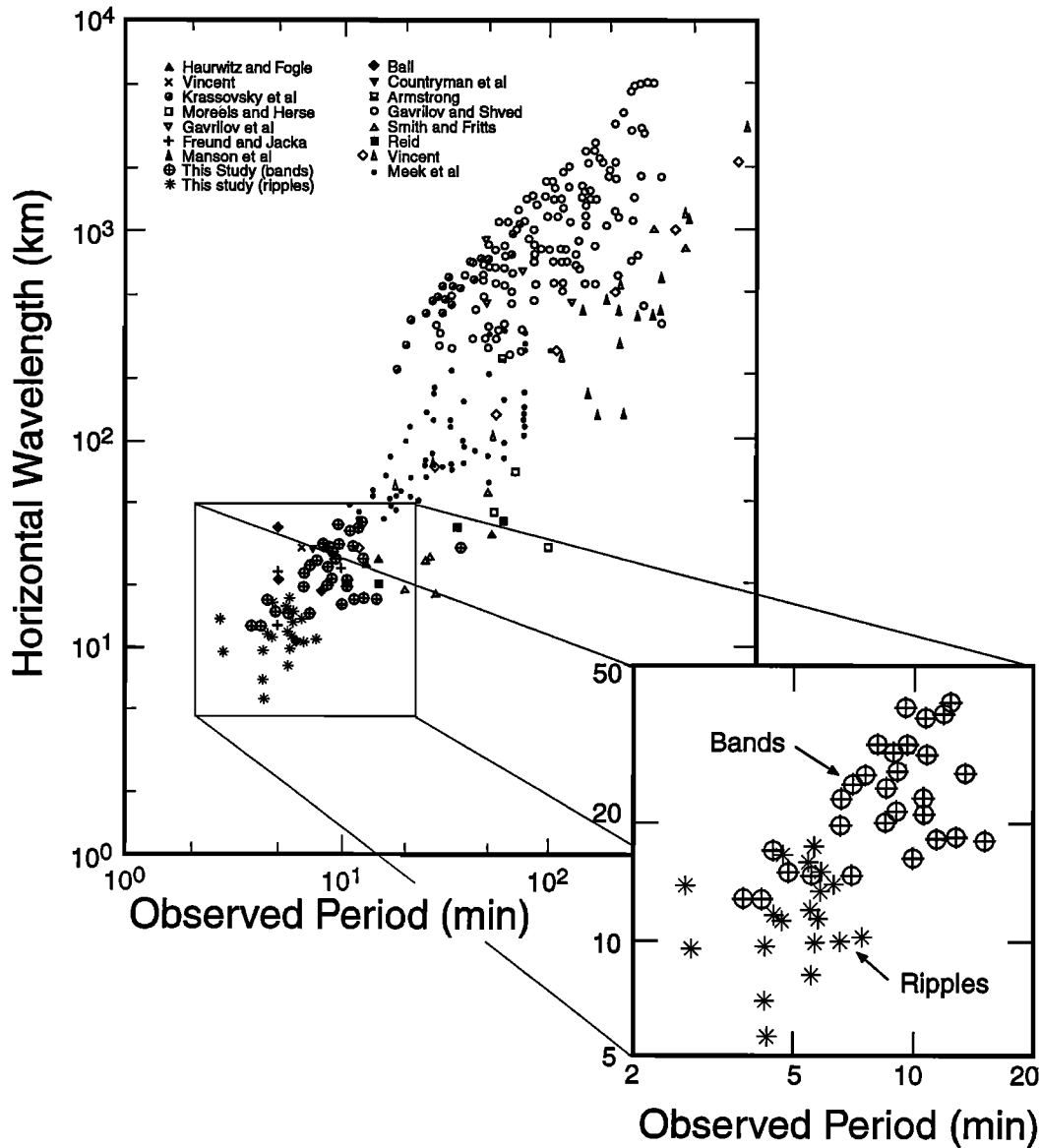
Figure 13. Comparison of the image measurements recorded during the Guara campaign with the collation of radar and optical measurements of horizontal wavelength versus observed period reported by *Reid* [1986]. The exploded view shows the Guara image component.

4.1. Comparison With Radar and Lidar Measurements

Figure 13 compares the results of our imaging study (49 events) with the collation of measurements of horizontal scale versus observed period reported by *Reid* [1986]. This data ensemble consists of a diverse set of 408 measurements 59% of which were derived from radar data and 41% from optical observations. The data are plotted on a log-log scale and span several decades in τ_{ob} and λ_h but are restricted significantly at short scales by the temporal and spatial resolution of the instrumentation and the observing configurations employed. The principal result of this study was the determination of a distinct trend toward longer horizontal wavelengths as the observed period of the waves increased. This data collation has subsequently been expanded greatly by the inclusion of MF Doppler radar measurements [*Reid and Vincent*, 1987] and MF triple bistatic (Gravnet) radar observations [*Manson and Meek*, 1988; *Manson*, 1990]. However, for simplicity we have chosen to

compare our results with Reid's original collation which is in excellent agreement with the more recent radar results, as noted by *Manson* [1990].

With one exception ($\tau_{ob} = 36.6$ min), all of our data fall within the square area outlined on the figure (which also includes several points from Reid's collation). The trends evident in the image data compare very favorably with those present in the ensemble of measurements (as shown in the exploded view which includes only the "Guara component"). It is clear that the imaging results provide an important addition to this collation of wave events in the region of short observed periods ($\tau_{ob} < 20$ min) and short horizontal wavelengths ($\lambda_h < 50$ km). This statement is also pertinent to the more extensive wave measurements reported by *Reid and Vincent* [1987], *Manson and Meek* [1988], and *Manson* [1990] which are characterized by observed periods ≥ 10 min and, in the latter two studies, by $\lambda_h \geq 40$ km. Since 22 of the band events in our study

exhibited observed periods ≤ 10 min and all had horizontal wavelength's ≤ 40 km, they complement substantially the larger data sets from the MF radar investigations.

In addition to comparison with the optical and radar collation of *Reid* [1986] the results of this study have also been compared with those from previous optical [*Krassovsky et al.*, 1977; *Gavrilov and Shved*, 1982; *Jacob and Jacka*, 1985], radar [*Meek et al.*, 1985], and lidar [*Gardner and Voelz*, 1987; *Beatty et al.*, 1992] studies. Figure 14 summarizes the $(\lambda_h - \tau_{ob})$ trends derived from these investigations. The early optical measurements (lines 1 and 2) yielded trends associated with relatively large horizontal wavelength waves $(\lambda_h > 200$ km) that are outside the nominal limits of detection for the image data. However, more recent radar and optical measurements (lines 3, 4, and 5) extend to much shorter horizontal scales (<50 km wavelength) and indicate comparable trends to that determined from our image data. In particular, the trend (line 6) associated with the image measurements ≥ 2 September $(\lambda_h = 3.1\tau_{ob}^{1.06})$ is in remarkable agreement with that deduced by *Reid* [1986] from his "global fit" $(\lambda_h = 3.62\tau_{ob}^{1.06})$ to a diverse set of measurements. In contrast, the $(\lambda_h - \tau_{ob})$ trends inferred from the lidar measurements [*Gardner and Voelz*, 1987; *Beatty et al.*, 1992] differ markedly from the radar/optical results, particularly in the small-τ_{ob} domain. For example, a wave exhibiting a τ_{ob} of ~ 10 min would be expected to have a horizontal wavelength ~ 30 km according to the image measurements, whereas its predicted λ_h would be over an order of magnitude smaller (~ 2 km) when based on the lidar results. Only at very long wave periods (several hours) and large horizontal scales (≥ 1000 km) do the values predicted by the radar and lidar trends become similar [e.g., *Nakamura et al.*, 1993; *Namboothiri et al.*, 1996]. The difference between radar and lidar measurements of gravity wave scales has been discussed in some detail by *Manson* [1990] and more recently by *Beatty et al.* [1992], but as indicated by both groups, a satisfactory explanation has yet to emerge.

For the short-period data under discussion here, one possible explanation for the disparity between the imager and lidar trends may have its basis in the fact that these two instruments tend to sample different parts of the gravity wave spectrum. It is important to reemphasize that an imager provides direct measurements of λ_h and v_h for short-period, quasi-monochromatic waves. In contrast, a lidar samples directly the vertical wave field from which the horizontal scales are inferred using the internal gravity wave (IGW) dispersion relationship [e.g., *Gardner and Voelz*, 1987]. Recently, *Taylor et al.* [1995c] have compared wave data recorded simultaneously by the University of Illinois wind-temperature lidar system and by the all-sky imager used for these studies. Distinct gravity wave signatures were observed simultaneously by both instruments on several occasions, yet comparison of a (limited) data set indicates that the waves detected by each system were quite different. The lidar measured short vertical wavelength waves (few kilometers) corresponding to large apparent horizontal wavelengths (~ 200 km), while the imager showed directly much shorter horizontal wavelength (~ 20 km) waves. The primary reason for this was determined to be the differing capabilities of the two instruments for sensing waves of different vertical scales. The lidar is most sensitive to short vertical wavelength waves ($\lambda_z \leq 10$ km) due to the finite width of the Na layer. In contrast, the imager is most responsive to wave events with vertical wavelengths greater than the width of the airglow layers (typically 6–10 km full width at half maximum (FWHM)).
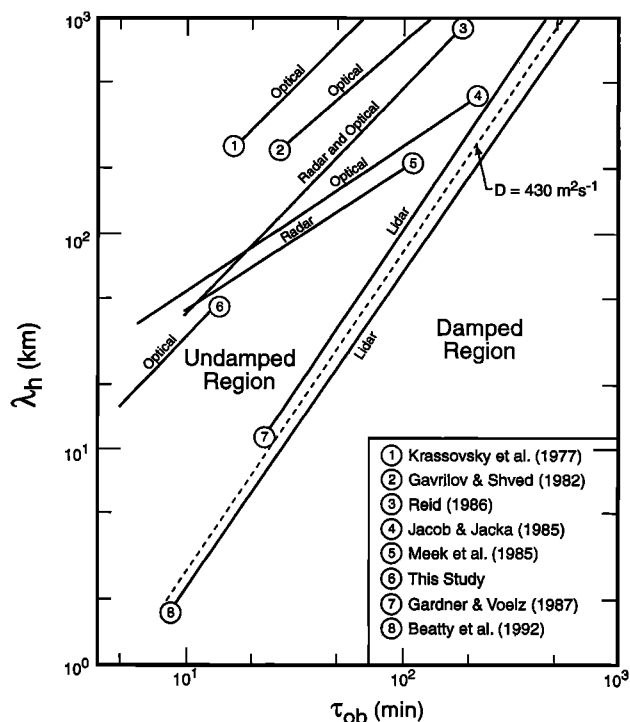

Figure 14. Summary plot showing the $(\lambda_h - v_h)$ trends derived from previous optical, radar, and lidar investigations. Trend 6 indicates the results of this imaging study. Note the dashed line indicates the diffusive damping limit determined from the scale independent diffusive filtering theory [*Gardner*, 1994] for a value of $D = 430$ m^2 s^{-1}.

Examination of the image data of Figure 15 (which presents values for the vertical wavelengths and intrinsic periods calculated using model winds discussed in seciton 4.2) support this conclusion as many of the waves imaged during the Guara campaign exhibited apparent vertical scales significantly larger than 10 km which would make them difficult to detect by lidar techniques. Thus as these two instruments tend to sample different parts of the gravity wave spectrum, it is not surprising that the data indicate different trends. The consequences of these differences require further investigation, but they are clearly important and should be borne in mind when comparing such data sets.

It has been suggested by *Collins et al.* [1996] that the Na lidars preferentially reveal waves which are very near the strong-diffusive-damping limit defined by *Gardner* [1994] in his scale-independent diffusive-filtering theory (SIDFT) for atmospheric gravity waves. In this theory the transition from undamped to damped wave motions is defined by the condition $\omega = m^2 D$, where $\omega =$ the intrinsic angular frequency; m is the vertical wave number $(2\pi/\lambda_z)$, and D is the total effective diffusivity of the atmosphere. This condition results when the effective vertical diffusion velocity (mD) of particles in the wave-carrying medium equals the vertical phase velocity, $v_z = \omega/m$, of the wave. Wave motions satisfying the inequality $mD > v_z$ are assumed to be severely damped, whereas those with v_z significantly larger than mD are considered undamped.

When the condition $\omega = m^2 D$ is used in the IGW dispersion relationship, the approximate expression $\lambda_h \cong (\sqrt{2\pi D/\tau_b})\tau_i^{1.5}$ follows provided the condition $(\tau_i/\tau_b)^2 \gg 1$ is satisfied. Here, τ_i denotes the intrinsic wave period $(2\pi/\omega)$,
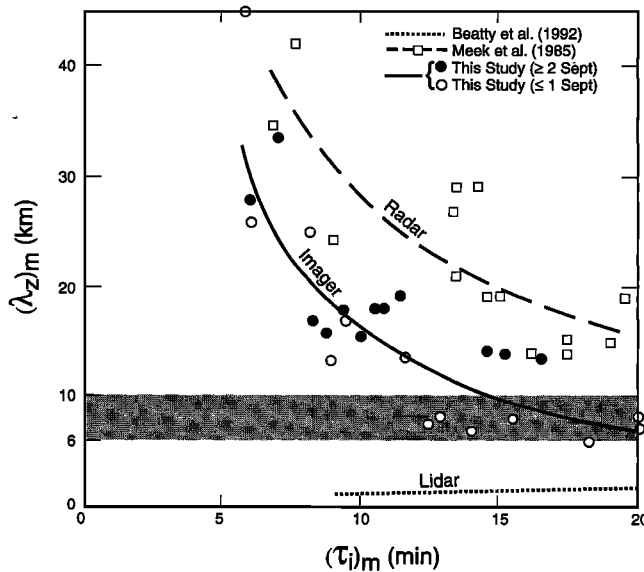
Figure 15. Plot showing the estimated vertical wavelength $(\lambda_z)_m$ for 26 band events as a function of their intrinsic period $(\tau_i)_m$ (solid curve) obtained using model wind data. For comparison the $(\lambda_h - \tau_i)$ radar data of *Meek et al.*, [1985] (long-dashed curve) and the $(\lambda_h - \tau_{ob})$ lidar data of *Beatty et al.* [1992] (dotted curve) are shown. The shaded area represents uncertainties in the depths of the emission layers (ranging from ~6 to 10 km full width at half maximum).

and τ_b is the Brunt-Vaisala period (see section 4.2). In Figure 14 the dashed line between the two lidar trends (7 and 8) represents the $(\lambda_h - \tau_{ob})$ relationship assuming $\tau_i = \tau_{ob}$ and using values of $D = 430$ m^2 s^{-1} and $\tau_b = 5.0$ min. This line of demarcation between the undamped (left of line) and damped (right of line) wave motions in the SIDF theory was chosen arbitrarily to lie approximately midway between the two lidar trends for clarity of presentation. (The values of D required to match lines 7 and 8 are ~550 m^2 s^{-1} and 350 m^2 s^{-1}, respectively.) The region to the left of the dashed line (undamped waves) contains all of the trend lines derived from optical and/or radar data. However, as noted by *Manson* [1990], a small but significant number of the radar-deduced wave events also occurred in the strong-damping region even when intrinsic parameters were used in their analysis. Concerning the optical measurements, nearly all of the reported wave events appear to lie well within the undamped region.

The SIDF theory provides a credible physical explanation for the highly significant trends ($r^2 \sim 0.97$) in the lidar results of *Gardner and Voelz* [1987] and *Beatty et al.* [1992] provided these systems preferentially select wave events at or very near the saturation limit for wave growth (i.e., large-amplitude waves). In comparison, the physical basis for the less significant but clearly apparent trends in the optical and radar results is not so evident. However, system and sampling limitations are expected to influence the trend analyses. We are currently investigating trends in the imager data using a larger ensemble of wave events resulting from measurements during other campaigns. Preliminary analysis of these data sets support the general $(\lambda_h - \tau_{ob})$ behavior deduced from the limited number of band events observed during the Guara campaign suggesting an inherent trend in the imager data. A possible "driver" for this trend in the (λ_h, τ_{ob}) image results is the finite thick-

ness of the airglow layers. In particular, cancellation effects within the layer are expected to limit the readily observable wave events to those which satisfy the condition $(\lambda_z/d) > 1$, where d represents the effective layer thickness [*Gavrilov and Shved*, 1982; *Schubert et al.*, 1991]. Thus waves with $\lambda_z < 6\text{-}10$ km (the typical FWHM of the emission layers) may be strongly damped, whereas waves of longer vertical wavelength would be essentially unaffected. A lower limit for λ_z implies a corresponding lower limit for λ_h, based on the dispersion relationship [*Hines*, 1960], and the lower limit for λ_h should increase with increasing intrinsic period. This hypothetical source for the trending in the imager results appears promising, but further analyses are needed to clarify this possibility.

4.2. Vertical Wavelength and Background Winds

In the presence of a background wind the observed wave period may differ significantly from its intrinsic period (τ_i) as a result of Doppler shifting by the background winds. The intrinsic period of the wave, measured in a frame of reference moving with the background wind, is related to the observed period through

$$\tau_i = \tau_{ob}(v_h)/(v_h - \bar{U}), \qquad (1)$$

where $\bar{U}$ is the component of the background wind in the direction of horizontal motion of the wave. Once τ_i is known for each event, the vertical wavelengths (λ_z) can then be investigated using the approximate dispersion relationship

$$\lambda_z \simeq (\lambda_h/\sqrt{(\tau_i/\tau_b)^2 - 1}). \qquad (2)$$

This relationship is valid for an isothermal, stationary atmosphere when both λ_h and λ_z are small compared to $C\tau_b$ (typically $C\tau_b \sim 100$ km), where C is the speed of sound and τ_b the Brunt-Vaisala period (or buoyancy period) of the atmosphere. For this study we have computed height-averaged values (~85-95 km) of τ_b based on the mean nocturnal rotational temperatures derived from the OH M (6, 2) and O$_2$ atmospheric (0, 1) emissions. These temperature measurements were obtained using a narrow field, tilting-filter photometer [*Takahashi et al.*, 1986] operated in close proximity to the all-sky imager at Alcantara by INPE personnel. The precise values of τ_b are not critical for this study in view of our use of model winds for the vertical wavelength calculations.

Unfortunately, coincident wind data are not available for the observation period of the imaging measurements. However, in situ rocket soundings of the stratospheric and mesospheric winds were made over a ~10-day period during the first part of the campaign (16-25 August) using the falling-sphere technique (F. Schmidlin, private communication, 1996). These measurements were made close to full moon when almost no image data were recorded and reveal relatively constant eastward (zonal) winds around 0-20 ms^{-1} at 85 km and a variable (~0-40 ms^{-1}) northward (meridional) wind component. (Data available at 90 km are less reliable and are not considered here.) To investigate the expected "mean" wind conditions during the primary data-taking interval, we have therefore used model results based on the MSIS model [*Hedin et al.*, 1993a, b] for this site and time of year. Estimates of the meridional and zonal wind components were obtained for three heights, 85, 90, and 95 km (corresponding closely to the centroids of the OH, Na, and OI emission layers) for each night by averaging over a 3-hour period centered on local midnight (M. Hagan, private communication, 1996). The model results at 95

km (where most of the waves were measured) indicate steadily increasing eastward winds rising from ~13 to 19 ms^{-1} during the campaign period. In comparison the meridional winds are <2 ms^{-1} southward during the first period but reverse to northward shortly before the second period and reach ~5 ms^{-1}. At 90 km the model predicts similar values for the zonal wind at ~15 ms^{-1}, but the meridional wind is northward decreasing steadily from ~15 to 5 ms^{-1} during the campaign period. Thus the model estimates relatively low wind speeds throughout the campaign in reasonable accord with the rocket measurements obtained earlier.

Because of the paucity of equatorial wind measurements from which this empirical model was formulated, these winds can, at best, only be considered as indicative of the true mean wind conditions. The computed estimates of τ_b and the derived parameters of $(\tau_i)_m$ and $(\lambda_z)_m$ using the model winds (as denoted by the subscript m) are listed in Table 2 together with the measured wave parameters. Despite the uncertainties these computations represent our best estimates of the vertical scales of the waves imaged during the Guara campaign. Examination of Table 2 indicates that the background winds had a significantly larger impact on the estimates of intrinsic periods for the waves imaged prior to 2 September, when the observed phase speeds were relatively low (mean value = 36.1 ms^{-1}), as compared with the second period when the wave phase speeds were much higher (mean value = 57.1 ms^{-1}) (see Figure 12). Assuming a well-defined trend in the intrinsic wavelength-period relationship for the image data, these results suggest that the effect of the background winds is to mask its appearance in the (λ_h, τ_{ob}) diagram. For example, during the first interval (≤1 September) the intrinsic wave periods differed significantly (up to about 80%) from the observed periods, and no obvious trend was discerned (see Figure 11b). However, for the second observing interval the difference between τ_i and τ_{ob} was often small (typically in the range -15% to 30%) due to the higher wave phase speeds, and a clear trend was found (Figure 11c). The overall trend for the campaign was very similar but less well defined and reflected a range of observing conditions. If this is the case, then (λ_h, τ_{ob}) trends should be most apparent under either very low wind conditions (i.e., around the equinox) or when $v_h \gg \bar{U}$ at the azimuth of wave progression.

This phenomenon has been noted by *Reid and Vincent* [1987] who investigated $(\lambda_h - \tau_{ob})$ trends using radar data obtained during various seasons. The individual plots clearly show a higher degree of correlation around the equinox periods, compared with those of other months, that was attributed to reduced winds. The trend associated with our (τ_{ob}, λ_h) pairs measured on and after 2 September $(\lambda_h = 3.14\tau_{ob}^{1.06})$ may therefore be more representative of the intrinsic period versus horizontal wavelength relationship. The remarkable agreement with the trend deduced by *Reid* [1986] from his global fit $(\lambda_h = 3.62\tau_{ob}^{1.06})$ is at first glance surprising. However, as Reid's collation reflects a wide variety of local times and seasonal conditions, the average power-law fit to this diverse set of measurements may therefore be more suggestive of an intrinsic trend.

Figure 15 presents our estimates of the vertical wavelengths associated with 26 of the band events versus $(\tau_i)_m$ on a linear scale. The same coding of events as used in previous figures is repeated here. These estimates are compared with a set of 14 intrinsic values deduced by *Meek et al.* [1985] (open squares) using simultaneous observations of mesospheric waves and

wind velocities recorded by the Gravnet MF radar system at Saskatoon (52°N). In addition, the measured $(\lambda_z - \tau_{ob})$ relationship (maximum likelihood power-law fit) obtained by *Beatty et al.* [1992] using Na lidar observations of 62 quasi-monochromatic gravity wave events observed in the vicinity of the mesopause over Arecibo, Puerto Rico (~18°N), is plotted (dotted line). A detailed comparison of trends associated with these three data sets is complicated by the differences in the system limits and in the case of the lidar measurements, by Doppler-shifting effects (as no estimates of the intrinsic periods were made). The Gravnet system limits are $\tau_{ob} \geq 10$ min and $\lambda_z \geq 20$ km at $\tau_i = 10$ min, decreasing to $\lambda_z \geq 10$ km at $\tau_i = 20$ min. The limits for the lidar measurements of interest are $\tau_{ob} \geq 4$ min and $\lambda_z \leq 20$ km [*Beatty et al.*, 1992]. In comparison, the limits associated with the imaging measurements are $\tau_{ob} \geq 2-3$ min and $\lambda_z \geq 6-10$ km, due to layer-thickness limitations (as discussed earlier).

The trend associated with the Gravnet results (long-dashed curve) exhibits a similar shape to that obtained in the present imaging study but is displaced toward longer vertical wavelengths. Both sets of measurements suggest significant vertical scales, ~15 km (imager) and ~25 km (radar) for an intrinsic wave period of 10 min. Furthermore, both curves indicate significantly larger vertical wavelengths near the Brunt-Vaisala period (~5 min), in accord with the expectation of near vertical energy propagation as this limit is approached. In sharp contrast, the lidar results (short-dashed curve) suggest a λ_z of only about 1 km at 10 min, with a decreasing trend continuing to near τ_b [*Beatty et al.*, 1992]. (Note that the shallow gradient of the lidar curve indicates that this conclusion is valid even under significant Doppler-shifting conditions.) Thus both the measured horizontal scale trends and the inferred vertical scale trends highlight a significant difference between the imager and the lidar data at short observed periods. The figure also shows that all of the wave events measured on and after 2 September (solid circles) exhibit values of $(\lambda_z)_m$ which are significantly greater than the nominal airglow layer thickness (indicated by the shaded band). In comparison, several events imaged earlier in the campaign (open circles) exhibit vertical scale sizes less than or similar to the nominal depth of the airglow layer where cancellation effects are expected to be significant [*Gavrilov and Shved*, 1982; *Schubert et al.*, 1991]. These wave events are characterized by relatively low phase speeds (mean value = 36.1 ms^{-1}) and are thus more susceptible to an increased uncertainty relating to the impact of background wind corrections for the λ_z calculations. The implications are that the model has most probably underestimated the actual mean wind conditions during this period. This suggestion is in good accord with the lack of a significant (λ_h, τ_{ob}) trend prior to 2 September.

4.3. Wave Sources

On the basis of the detection of a major change in the azimuthal distribution of the waves (Figure 8) the image data were divided into two sets covering the periods 6 August to 1 September (prior to the equinox) and 2 September to 16 October (around the equinox). One likely possibility for the apparent predominance for wave propagation toward ~NE-ENE is that seasonal changes in the stratospheric and mesospheric wind fields occurred during this time resulting in large changes in the filtering of the gravity wave spectrum. A second possibility is that a powerful wave source may have developed to the ~SW-WSW of Alcantara (over the South American continent)
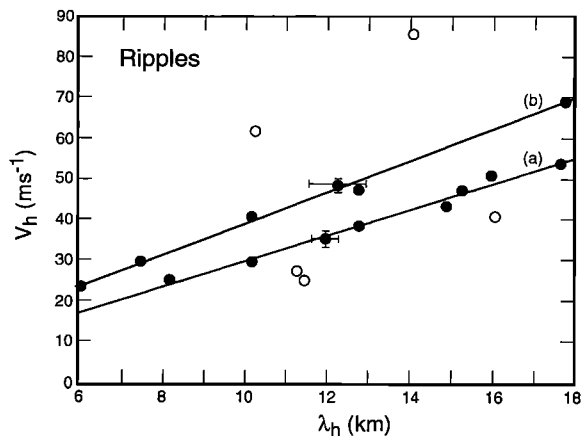
Figure 16. Plot of the ripple data of Figure 9 showing the bimodal distribution of the data: Line a indicates a wave period of 5.18 ± 0.26 min close to the Brunt-Vaisala period while line b has a period of 4.32 ± 0.15 min close to the acoustic cutoff period. An example error bar is given for each line to emphasize the distinction between the two trends. Note that only the points which comprised the central peak of the histogram distribution of Figure 6 were used in the trend analysis.

around 2 September. Wind filtering has been shown to play an important role in governing the azimuthal flux of wave energy penetrating into the upper atmosphere through the formation of critical layers [e.g., Ebel et al., 1987; Taylor et al., 1993]. For the Guara campaign a reduction in amplitude of the prevailing winds in the stratosphere and lower mesosphere associated with seasonal changes around the equinox could have opened a "window" permitting wave propagation into the upper mesosphere from sources located over the South American continent. This hypothesis supports the appearance of strong directionality in the wave headings around the equinox period. Alternatively, it is possible that the marked anisotropy in the wave motions may reflect changes in the prevailing flux of gravity waves into the mesosphere from, for example, an ensemble of freely propagating and/or ducted waves that could have originated from a variety of sources to a predominance for waves generated by a "local" tropospheric source located over the South American continent. In either case, the frequent recurrence of wave progression toward the equator on an ~NE-ENE heading indicates that the source region was active for a considerable period of time (persisting throughout September and early October). One possible candidate for the wave source is the Andes mountain range. This is favorably located to the W and SW of Alcantara but at a very large distance of ≥3000 km. In the absence of background winds, short-period (<1 hour) gravity waves generated near the Earth's surface would not be expected to propagate large horizontal distances (a few hundred kilometers) before they

reached the airglow layers [Hines, 1967]. However, if the prevailing stratospheric and mesospheric winds acted to increase the intrinsic periods of the waves progressing toward the ~NE-ENE during this interval, then the horizontal distance traveled by these waves, prior to reaching the airglow layers, could have increased significantly [e.g., Taylor and Edwards, 1991]. Another possibility is that upon reaching airglow altitudes, the waves may have become ducted by the mesospheric background winds further increasing their range of propagation from the source region. Thus although the Andes mountains are at an extreme range, they are a potentially good candidate. An alternative potential source is strong tropospheric convection over central Brazil. The dominant source (or sources) of these waves remains unknown at the present time but is under investigation.

4.4. Ripple Periodicities

The sharp distribution in observed periodicities of the ripple events (Figure 6b) (average τ_{ob} = 5.1 min, range 2.7–6.9 min) is a characteristic property that has not been reported previously. As expected, the ripples exhibited shorter horizontal wavelengths (range typically 5–15 km) than bands. However, they were also found to exhibit a significantly different distribution than the bands when plotted in the $(\lambda_h - \tau_{ob})$ format. This is illustrated in Figure 10 which shows the ripples clustered around the mean observed period of ~5 min and exhibiting no obvious $(\lambda_h - \tau_{ob})$ trend. These properties set ripples apart from most band displays. In particular, the bimodal form of the $(\lambda_h - v_h)$ distribution evident in the ripple data of Figure 9 is most unusual. Figure 16 replots the ripple data of Figure 9 on an expanded scale to investigate this phenomenon. In Figure 16 no attempt has been made to distinguish between ripples observed prior to or after 2 September (as no association was found). Out of a total of 19 events, 14 were found to be associated with two well-defined trend lines. The distinct nature of these two trends is emphasized by the example error bars in each case.

A regression analysis was carried out following procedures similar to those described by Wonnacott and Wonnacott [1981]. The results of this analysis (which uses only the 14 events associated with the central peak in Figure 6) are summarized in Table 5, where the parameters A and B for linear fits of the form $v_h = A + B\lambda_h$ are given together with confidence limits and the squared correlation coefficients (r^2). The table shows that "A" appears to be zero to within 1σ for both trend lines, suggesting a more simplified relation $v_h = B\lambda_h$. These linear relationships correspond to highly significant trends $(r^2 = 0.990)$. Thus despite the relatively small number of events associated with each trend $(N = 6 \text{ and } 8)$, the relationships are significant at a confidence level of about 0.01%. The apparent frequencies associated with these two trend lines are 3.22 ± 0.16 mHz and 3.86 ± 0.13 mHz which correspond to observed periods of 5.18 ± 0.26 min and 4.32 ± 0.15 min.

Table 5. Results of Trend Analysis for Ripple Data of Figure 16 (Using 14 Points Associated With the Central Peak of Figure 6)

Ripples	Coefficient, A	Frequency, B, mHz	Correlation Coefficient Squared, r^2	Total Data Pairs, N	τ_{ob}, min
Line a	−2.34 ± 2.25	3.22 ± 0.16	0.986	8	5.18 ± 0.26
Line b	0.44 ± 1.54	3.86 ± 0.13	0.996	6	4.32 ± 0.15

Parameters A and B were determined by fitting to the linear equation $v_h = A + B\lambda_h$.

It is interesting to note that these values for τ_{ob} are very close to those identified with the limits for the gravity wave (Brunt-Vaisala) and acoustic wave regimes in the IGW dispersion relationship. For an isothermal, stationary atmosphere, IGW theory predicts that there is a gap between the acoustic regime and the gravity wave regime (defined by these two limits) where no wave propagation occurs. Examination of Figure 16 reveals a distinct "gap" between the two trend lines where no data points are found. The uncertainties in the measurements (indicated by the example error bars) are insufficient to bridge this gap. Thus one possible interpretation consistent with the determination of two distinct trends is that the ripple patterns imaged during the Guara campaign comprised wave motions generated within the acoustic branch as well as the gravitational branch of the IGW spectrum. However, this interpretation appears to be in conflict with the expectation of much higher phase speeds at acoustic wave periods [Hines, 1960]. As the effect of background winds on the wave motions (assuming they are generated in situ) would be to fill in this gap, and because many of the ripple events exhibited relatively high phase speeds (>40 ms^{-1}), it is unlikely that Doppler shifting effects can account for the observed bimodal distribution. No obvious differences in morphology of the wave motions comprising this bimodal distribution were found, and it remains to be seen if it is also evident in other more substantial midlatitude ripple measurements that are currently under analysis.

Ripples are similar in morphology and dynamics to the billow-type waves seen in noctilucent clouds many of which are thought to be generated in situ by short-lived velocity shears (≥ 40 ms^{-1} km^{-1}) in the background winds [Taylor and Hapgood, 1990]. Waves generated by this mechanism (Kelvin-Helmholtz instability) would be expected to exhibit observed periods close to the local Brunt-Vaisala period and would have variable and limited lifetimes (depending on the duration of the shear). Alternatively, it is possible that ripples are generated in situ by the breakdown of a larger-scale wave (possibly of tidal origin) either through parametric excitation [Tuan et al., 1979] or by the onset of a three-dimensional convective-type instability [e.g., Fritts et al., 1993]. In the latter case, the orientation of the ripples would be expected to be near perpendicular to the large-scale perturbing wave. Isolated ripple-type patterns oriented almost orthogonal to large-scale band patterns were observed on several occasions during the Guara campaign, suggesting a causal relationship. However, Fritts et al. [1996] have recently modeled the generation of ripple-type waves using data obtained during the CORN campaign and have determined that the scale size of the perturbing (breaking) wave should be much larger than that of the bands. In general, ripples of scale-sizes ($\lambda_h > 5$ km) and lifetimes ($>$several minutes), which typify most events, are currently not thought to be compatible with the convective instability theory. Without further information it is not possible to distinguish between these potential mechanisms.

Finally, Witt [1962] suggested that if NLC billows are generated in situ, they will tend to move with the background wind. NLC bands, on the other hand, may be expected to progress in any direction provided their horizontal phase speed exceeds the background wind speed [Ebel et al., 1987; Taylor et al., 1993]. Assuming ripples are generated in situ, then their average motions may provide some information on the prevailing wind conditions in the 80–100 km region. As already mentioned, wind measurements were not performed during the period when most of the image data were obtained. However, the dominance of eastward propagating components for the ripples observed throughout the campaign (Figure 8) is remarkably consistent with zonal flow predicted by the MSIS model. Furthermore, the observed reversal in the meridional wave progression from southward to northward during the campaign is also consistent with the modeled winds at the 95 km level. The magnitudes of the predicted winds are, however, generally smaller than the observed wave speeds, and it remains to be seen whether ripples are strongly influenced by the background wind. Indeed, several of the ripple events recorded during the second observing interval progressed in approximately the same direction ($\sim$NE-ENE) as the band displays, suggesting a common origin.

5. Summary

Statistical measurements of short-period gravity waves are few and this data set, comprising over 50 events, represents a major first step in quantifying the occurrence frequency and properties of small-scale gravity waves present at equatorial latitudes. Analysis of these data indicates two apparently separable wave sets, termed bands and ripples, and a marked anisotropy in the distribution of wave headings around the equinox with a large fraction ($>65\%$) of the band-type wave motions progressing toward the equator on an $\sim$NE-ENE heading.

Comparison of these wave data with more extensive measurements obtained by radar and lidar techniques in recent years indicates a similar tendency for the observed period of the waves to increase with increasing horizontal wavelength. In particular, the ($\tau_{ob} - \lambda_h$) trend determined from the band data recorded around the equinox period agrees very well with that deduced by Reid [1986] using a diverse collation of radar and optical measurements. As the imaging system is most sensitive to waves of a smaller horizontal scale than those readily detected by radar, these measurement techniques are highly complementary. However, a similar comparison with the lidar data indicates considerable differences that exceed an order of magnitude at short τ_{ob}. The reasons for this discrepancy are thought to be related to the differing sensitivities of the two instruments to waves of different vertical scale sizes, but further joint research is necessary to investigate this effect.

It is conjectured that the high degree of correlation in the measurements obtained around the equinox may have resulted from a reduction in the stratospheric and mesospheric winds associated with seasonal changes. However, it remains to be seen how the trends observed in this data set (limited to $\sim$2 months) compare with results of other more substantial image measurements obtained during different seasons. The onset of a series of highly directional wave motions during this period also appears to be associated with equinox conditions. One potential source for the large flux of waves observed on an $\sim$NE-ENE heading may be associated with strong winds blowing over the Andes mountain range. However, an investigation of the penetration of wave energy into the mesosphere at equatorial latitudes and of potential tropospheric sources for these waves will be the subject of a separate report.

Short-period mesospheric wave motions have now been observed from a number of middle and low-latitude sites around the world. The data presented here, using a high-resolution CCD imager, contribute significantly to the "global picture" by revealing a wealth of wave structure at equatorial latitudes.

The band displays were usually (but not always) observed in all three of the nightglow emissions imaged (OI, Na, and OH), indicating freely propagating or ducted wave behavior. In comparison, the ripples were often present in only one of the three emissions, consistent with the hypothesis of in situ generation over a limited height range. However, the Guara data indicate a considerable region of overlap in the spatial and temporal scales of the bands and ripples, and the additional information provided by the imager (e.g., geographic extent and pattern lifetimes) was often necessary to distinguish accurately between these two groups. This distinction between waves generated in situ at airglow altitudes and those whose sources reside naturally in the lower atmosphere is an essential first step toward estimating the flux of quasi-monochromatic gravity waves into the mesosphere and lower thermosphere and their associated momentum deposition.

References

Armstrong, E. B., The association of visible airglow features with a gravity wave, *J. Atmos. Terr. Phys.*, *44*(4), 325, 1982.

Armstrong, E. B., Irregularities in the 80–100 km region: A photographic approach, *Radio Sci.*, *21*(3), 313, 1986.

Baker, D. J., and A. T. Stair Jr., Rocket measurements of the altitude distributions of the hydroxyl airglow, *Phys. Scr.*, *37*, 611, 1988.

Beatty, T. J., C. A. Hostetler, and C. S. Gardner, Lidar observations of gravity waves and their spectra near the mesopause and stratopause at Arecibo, *J. Atmos. Sci.*, *49*(6), 477, 1992.

Clairemidi, J., M. Herse, and G. Moreels, Bi-dimensional observations of waves near the mesopause at auroral latitudes, *Planet. Space Sci.*, *33*(9), 1013, 1985.

Collins, R. L., X. Tao, and C. S. Gardner, Gravity wave activity in the upper mesosphere over Urbana, Illinois: Lidar observations and analysis of gravity wave propagation models, *J. Atmos. Terr. Phys.*, *58*, 1905, 1996.

Ebel, A., A. H. Manson, and C. E. Meek, Short period fluctuations of the horizontal wind measured in the upper atmosphere and possible relationships to internal gravity waves, *J. Atmos. Terr. Phys.*, *49*, 385, 1987.

Fagundes, P. R., H. Takahashi, Y. Sahai., and D. Gobbi, Observations of gravity waves from multispectral mesospheric nightglow emissions observed at 23°S, *J. Atmos. Terr. Phys.*, *57*(4), 395, 1995.

Fritts, D. C., and R. A. Vincent, Mesospheric momentum flux studies at Adelaide, Australia: Observations and gravity wave-tidal interaction model, *J. Atmos. Sci.*, *44*, 605, 1987.

Fritts, D. C., J. R. Isler, G. E. Thomas, and Ø. Andreassen, Wave breaking signatures in noctilucent clouds, *Geophys. Res. Lett.*, *20*(19), 2039, 1993.

Fritts, D. C., J. R. Isler, J. H. Hecht, R. L. Walterscheid, and Øyvind Andreassen, Wave breaking signatures in sodium densities and OH nightglow, 2, Simulation of wave and instability structures, *J. Geophys. Res.*, in press, 1996.

Gardner, C. S., Diffusive filtering theory of gravity wave spectra in the atmosphere, *J. Geophys. Res.*, *99*, 20,601, 1994.

Gardner, C. S., and D. G. Voelz, Lidar studies of the nighttime sodium layer over Urbana, Illinois, 2, Gravity waves, *J. Geophys. Res.*, *92*, 4673, 1987.

Gavrilov, N. M., and G. M. Shved, Study of internal gravity waves in the lower thermosphere from observations of the nocturnal sky airglow [OI] 5577 Å in Ashkhabad, *Ann. Geophys.*, *38*(6), 789, 1982.

Goldberg, R. A., M. Friedrich, G. A. Lehmacher, F. J. Schmidlin, C. L. Croskey, J. D. Mitchell, D. C. Fritts, and W. E. Swartz, MALTED: A rocket/radar study of dynamics and turbulence in the equatorial mesopause region, in *Proceedings of the 12th ESA Symposium on Rocket and Balloon Programs and Related Research*, ESA SP-370, p. 113, Eur. Space Agency, Neuilly, France, 1995.

Hapgood, M. A., and M. J. Taylor, Analysis of airglow image data, *Ann. Geophys.*, *38*(6), 805, 1982.

Haurwitz, B., and B. Fogle, Wave forms in noctilucent clouds, *Deep Sea Res.*, *16*, 85, 1969.

Hedin, A. E., E. L. Fleming, A. H. Manson, F. J. Schmidlin, S. K. Avery, and S. J. Franke, Empirical wind model for the middle and lower atmosphere, 1, Local time average, *NASA Tech. Memo. 104581*, 1993a.

Hedin, A. E., et al., Empirical wind model for the middle and lower atmosphere, 2, Local time variations, *NASA Tech. Memo. 104592*, 1993b.

Herse, M., G. Thuillier, G. Camman, J.-L. Chevassut, and M. Fehrenbach, Ground based instrument for observing near IR nightglow inhomogeneities at zenith and throughout the sky, *Appl. Opt.*, *28*, 3944, 1989.

Hines, C. O., Internal atmospheric gravity waves at ionospheric heights, *Can. J. Phys.*, *38*, 1441, 1960.

Hines, C. O., On the nature of traveling ionospheric disturbances launched by low-altitude nuclear explosions, *J. Geophys. Res.*, *72*, 1877, 1967.

Jacob, P. G., and F. Jacka, Gravity wave vertical energy flux at 95 km, in *Proc. MAP Handb.*, *18*, 248, 1985.

Krassovsky, V. I., B. P. Potapov, A. I. Semenov, M. V. Shagaev, N. N. Shefov, V. G. Sobolev, and T. I. Toroshelidze, Internal gravity waves near the mesopause and the hydroxyl emission, *Ann. Geophys.*, *33*(3), 347, 1977.

Manson, A. H., Gravity wave horizontal and vertical wavelengths: An update of measurements in the mesopause region (~80–100 km), *J. Atmos. Sci.*, *47*(23), 2765, 1990.

Manson, A. H., and C. E. Meek, Gravity wave propagation characteristics (60–120 km) as determined by the Saskatoon MF radar (Gravnet) system; 1983–85 at 52°N, 107°W, *J. Atmos. Sci.*, *45*, 932, 1988.

Meek, C. E., I. M. Reid, and A. H. Manson, Observations of mesospheric wind velocities, 1. Gravity wave horizontal scales and phase velocities determined by spaced wind observations, *Radio Sci.*, *20*, 1363, 1985.

Moreels, G., and M. Herse, Photographic evidence of waves around the 85 km level, *Planet. Space Sci.*, *25*, 265, 1977.

Nakamura, T., T. Tsuda, M. Yamamoto, S. Fukao, and S. Kato, Characteristics of gravity waves in the mesosphere observed with the middle and upper atmosphere radar, 2, Propagation direction, *J. Geophys. Res.*, *98*, 9811, 1993.

Namboothiri, S. P., T. Tsuda, M. Tsutsumi, T. Nakamura, C. Nagasawa, and M. Abo, Simultaneous observations of mesospheric gravity waves with the MU radar and sodium lidar, *J. Geophys. Res.*, *101*, 4057, 1996.

Peterson, A. W., Airglow events visible to the naked eye, *App. Opt.*, *18*, 3390, 1979.

Peterson, A. W., and G. W. Adams, OH airglow phenomena during the 5–6 July 1982 total lunar eclipse, *App. Opt.*, *22*, 2682, 1983.

Reid, I. M., Gravity wave motions in the upper middle atmosphere (60–110 km), *J. Atmos. Terr. Phys.*, *48*(11–12), 1057, 1986.

Reid, I. M., and R. A. Vincent, Measurements of the horizontal scales and phase velocities of short period mesospheric gravity waves at Adelaide, Australia, *J. Atmos. Terr. Phys.*, *49*, 1033, 1987.

Schubert, G., R. L. Walterscheid, and M. P. Hickey, Gravity wave-driven fluctuations in OH nightglow from an extended, dissipative emission region, *J. Geophys. Res.*, *96*, 13,869, 1991.

Swenson, G. R., and S. B. Mende, OH emission and gravity waves (including a breaking wave) in all-sky imagery from Bear Lake, UT., *Geophys. Res. Lett.*, *21*, 2239, 1994.

Swenson, G. R., M. J. Taylor, P. J. Espy, C. Gardner, and X. Tao, ALOHA-93 measurements of intrinsic AGW characteristics using

airborne airglow imager and ground-based Na wind/temperature lidar, *Geophys. Res. Lett.*, *22*, 2841, 1995.

Takahashi, H., Y. Sahai, and P. P. Batista, Airglow $O_2(^1\Sigma)$ atmospheric band at 8645Å and the rotational temperature observed at 23°S, *Planet. Space Sci.*, *34*, 301, 1986.

Taylor, M. J., TV observations of mesospheric wave structure, *in Collection of Works of the International Workshop of Noctilucent Clouds*, 153, Valgus, Tallinn, 1986.

Taylor, M. J., and R. Edwards, Observations of short period mesospheric wave patterns: In situ or tropospheric wave generation?, *Geophys. Res. Lett.*, *18*(7), 1337, 1991.

Taylor, M. J., and F. J. Garcia, A two-dimensional spectral analysis of short period gravity waves imaged in the OI(557.7 nm) and near infrared OH nightglow emissions over Arecibo, Puerto Rico, *Geophys. Res. Lett.*, *22*(18), 2473, 1995.

Taylor, M. J., and M. A. Hapgood, Identification of a thunderstorm as a source of short period gravity waves in the upper atmospheric nightglow emissions, *Planet. Space Sci.*, *36*(10), 975, 1988.

Taylor, M. J., and M. A. Hapgood, On the origin of ripple-type wave structure in the OH nightglow emission, *Planet. Space Sci.*, *38*(11), 1421, 1990.

Taylor, M. J., and M. J. Hill, Near infrared imaging of hydroxyl wave structure over an ocean site at low latitudes, *Geophys. Res. Lett.*, *18*(7), 1333, 1991.

Taylor, M. J., M. A. Hapgood, and P. Rothwell, Observations of gravity wave propagation in the OI(557.7 nm), Na(589.2 nm) and the near infra-red OH nightglow emissions, *Planet. Space Sci.*, *35*(4), 413, 1987.

Taylor, M. J., E. H. Ryan, T. F. Tuan, and R. Edwards, Evidence of preferential directions for gravity wave propagation due to wind filtering in the middle atmosphere, *J. Geophys. Res.*, *98*(A4), 6047, 1993.

Taylor, M. J., M. B. Bishop and V. Taylor, All-sky measurements of short period waves imaged in the OI(557.7 nm), Na (589.2 nm) and near infrared OH and $O_2(0, 1)$ nightglow emissions during the ALOHA-93 campaign, *Geophys. Res. Lett.*, *22*(20), 2833, 1995a.

Taylor, M. J., V. Taylor, and R. Edwards, An investigation of thunderstorms as a source of short period mesospheric gravity waves, *in The Upper Mesosphere and Lower Thermosphere: A Review of Experiment and Theory, Geophys. Monogr., Ser.*, vol. 87, edited by R. M. Johnson and T. L. Killeeu, p. 177, AGU, Washington, D. C., 1995b.

Taylor, M. J., Y. Y. Gu, X, Tao, C. S. Gardner, and M. B. Bishop, An investigation of intrinsic gravity wave signatures using coordinated lidar and nightglow image measurements, *Geophys. Res. Lett.*, *22*(20), 2853, 1995c.

Tuan, T. F., R. Hedinger, S. M. Silverman, and M. Okuda, On gravity wave induced Brunt-Vaisala oscillations, *J. Geophys. Res.*, *84*, 393, 1979.

Witt, G., Height, structure and displacements of noctilucent clouds, *Tellus*, *24*, 1, 1962.

Wonnacott, T. H., and R. J. Wonnacott, Regression: A second course in statistics, John Wiley, New York, 1981.

World Meteorological Organization (WMO), *International Noctilucent Cloud Observation Manual, WMO-250.TP.138*, Geneva, 1970.

S. Clark, W. R. Pendleton Jr., and M. J. Taylor, Space Dynamics Laboratory and Physics Department, Engineering Building, Room 241, Utah State University, Logan, UT 84322. (e-mail: taylor@psi.sci.SDL.usu.edu)

D. Gobbi and H. Takahashi, Instituto Nacional de Pesquisas Espaciais, INPE, C.P. 515, 12201-970, São José dos Campos, São Paulo, Brazil.

R. A. Goldberg, Laboratory for Extraterrestrial Physics, NASA Goddard Space Flight Center, MD 20771.